

Machine learning methods to predict the fatigue life of selectively laser melted Ti6Al4V components

*Original*

Machine learning methods to predict the fatigue life of selectively laser melted Ti6Al4V components / Centola, Alessio; Ciampaglia, Alberto; Tridello, Andrea; Paolino, Davide Salvatore. - In: FATIGUE & FRACTURE OF ENGINEERING MATERIALS & STRUCTURES. - ISSN 8756-758X. - 46:11(2023), pp. 4350-4370. [10.1111/ffe.14125]

*Availability:*

This version is available at: 11583/2989416 since: 2024-06-11T09:48:10Z

*Publisher:*

WILEY

*Published*

DOI:10.1111/ffe.14125

*Terms of use:*

This article is made available under terms and conditions as specified in the corresponding bibliographic description in the repository

*Publisher copyright*

(Article begins on next page)

# Machine learning methods to predict the fatigue life of selectively laser melted Ti6Al4V components

Alessio Centola  | Alberto Ciampaglia | Andrea Tridello  |  
Davide Salvatore Paolino 

Department of Mechanical and Aerospace Engineering, Politecnico di Torino, Torino, Italy

## Correspondence

Alessio Centola, Department of Mechanical and Aerospace Engineering, Politecnico di Torino, Torino, 10129 Italy.  
Email: [alessio.centola@polito.it](mailto:alessio.centola@polito.it)

[Correction added on October 5, 2023, after first online publication: Article category corrected from “Original Article” to “Special Issue Article”.]

## Abstract

The aim of the present paper is to predict the fatigue life of Selectively Laser Melted (SLMed) Ti6Al4V components via the process parameters, the thermal treatments, the surface treatments and the stress amplitude, adopting machine learning techniques to reduce the cost of further fatigue testing, and to deliver better predictive fatigue designs. The studies resulted in reliable algorithms capable of predicting trustful fatigue curves. The methods have been trained with experimental data available in the literature and validated on testing sets to assess the extrapolation limits and to compare the different methods. The behavior of the networks has also been mapped by varying one SLM process parameter at the time, highlighting how each one affects the life.

## KEYWORDS

additive manufacturing, fatigue, machine learning, neural networks, physics informed, selective laser melting, Ti6Al4V

## Highlights

Machine learning can be used to reduce time and costs for fatigue characterization.

Machine learning predicts the life of SLMed Ti6Al4V specimens effectively. The physics informed neural network performs best.

## 1 | INTRODUCTION

It is widely known that Titanium alloys are difficult to work with traditional manufacturing processes, like the machining process. Indeed, titanium alloys are much harder to shape with traditional methods because they are not capable of conducting heat efficiently.<sup>1</sup> This

means that the cutting tool will absorb nearly all the heat that is generated during manufacturing, causing it to be degraded sooner.<sup>1</sup> Titanium is also tough, and a high shear force is needed to create a chip. These reasons make machining titanium tedious and expensive.<sup>1</sup> Moreover, Titanium alloys are used in biomedical applications,<sup>2</sup> whose parts and implants are of complicated

This is an open access article under the terms of the [Creative Commons Attribution-NonCommercial-NoDerivs](https://creativecommons.org/licenses/by-nc-nd/4.0/) License, which permits use and distribution in any medium, provided the original work is properly cited, the use is non-commercial and no modifications or adaptations are made.

© 2023 The Authors. *Fatigue & Fracture of Engineering Materials & Structures* published by John Wiley & Sons Ltd.

and often personalized shapes. Additive Manufacturing (AM) processes, on the other hand, allow to overcome these issues. Basically, it is based on adding material layer by layer, where each layer is connected via thermal bonding to the next and the previous one, up until the desired shape is reached. Aside from being able to manufacture complex parts, another significant advantage is that the AM processes allow to produce complex shapes without intermediate manufacturing operations. Accordingly, the mechanical performance of Ti6Al4V parts produced through AM processes should be carefully experimentally assessed and verified to ensure a safe design. Among the Titanium alloys produced with AM processes, the Ti6Al4V alloy is the most widespread and generally used in Selective Laser Melting (SLM) processes. Despite being characterized by good quasi-static mechanical properties, SLM Ti6Al4V parts showed a worse fatigue response, if compared to that of parts produced with traditional manufacturing processes. For example, the fatigue performances of as-fabricated (AF) SLMed specimens are generally worse than traditionally built ones.<sup>3,4</sup> Indeed, several factors affect the fatigue response. Among those, the combination of process parameters<sup>5</sup> plays the most important role. Indeed, the poor fatigue behavior of SLM Ti6Al4V AF parts can be mainly ascribed to the formation of defects during the layer-by-layer manufacturing process, like lack of fusions (LOF) defect or porosities, since they act as nucleation sites.<sup>5,6</sup> The part microstructure is also influenced by the combination of process parameters, even if heat treatments can induce microstructural variation affecting the fatigue performance.<sup>7</sup> Post-processing treatments can also affect the fatigue response. For example, to reduce the defect size, thermal treatments, such as hot isostatic pressing (HIP), are often employed.<sup>6,8–10</sup> Similarly, surface treatments like laser shot peening (LSP),<sup>11</sup> shot peening (SP),<sup>12,13</sup> polishing, surface mechanical attrition treatment (SMAT),<sup>14</sup> surface machining and sand blasting (SB)<sup>15</sup> can remove surface defects, improving the response to cyclic loads. Due to these large number of factors, the design against fatigue loads of SLM Ti6Al4V parts can be rather difficult.<sup>5,6,8,9,11,15–22</sup> Methodologies allowing to consider the influence of the above-described factors on the fatigue response would facilitate the design process, without compromising the part safety. Machine learning (ML) algorithms can help to manage problems where many input factors are present and the experimental response is significantly influenced by their interactions. Accordingly, they can be reliably used even for the design of parts to be produced with AM processes which are expected to withstand fatigue loads. This unlocks great potentialities for the fatigue design of SLM components, allowing to significantly reduce the time and the cost of

the experimental activity, provided that the ML algorithm is properly designed and validated. Indeed, literature data can be used to train the network, allowing to cut the time behind testing and to exhaustively map the connections between the specimen life and the factors influencing it. In the last decade, new ML approaches have been successfully applied to traditional fatigue fields, such as welding applications<sup>23,24</sup> and traditional steel LCF life characterization.<sup>25–27</sup> When it comes to AM, this research field is relatively new, even if in the last 2 years the number of research has increased for several SLM materials. In Sharma et al.,<sup>28</sup> a data-driven approach has been developed to predict the static properties of AM Ti6Al4V in which the Authors analyzed several additive manufacturing technologies, like SLM and direct metal laser sintering (DMLS). Liu and Chen<sup>29</sup> have used another training approach with probabilistic guided learning, with a smaller database and a Probabilistic Physics-guided Neural Network (PPgNN) to demonstrate the feasibility of the method. However, these first two approaches have datasets with missing process parameters in the training, while the research proposed in this paper has a fully populated Training DataBase (TDB) with a higher number of samples. Hornas et al.<sup>30</sup> carried out fatigue tests on 29 specimens to create a ML framework to solve the influence of defects and stress amplitude on the life of AM Ti6Al4V using artificial neural network (ANN), random forest regressor (RFR) and support vector regressor (SVR) models that validated the research. Ciampaglia et al.<sup>31</sup> have developed ML algorithms to estimate the fatigue response from the process parameters and heat treatment properties with a Physics Informed Neural Network (PINN) designed and validated on the literature of AM AlSi10Mg alloy. Salvati et al.<sup>32</sup> proposed an approach to predict the fatigue finite life of defective materials, again with a PINN, whose training process has been reinforced by introducing fracture mechanics constraints. Cutolo et al.<sup>33</sup> developed methods and results to predict the fatigue life of laser power bed fused complex shaped parts, using a finite element approach, stress-based sample fatigue data and an ML algorithm, to understand the fatigue performance of complex objects. Wang et al.<sup>34</sup> constructed an ML framework based on sensitive features and continuous damage mechanics to predict the fatigue life of AM AlSi10Mg parts, that also reduced the effect of causality among the features. Bagherifard et al.<sup>35</sup> analyzed the fracture surfaces of failed V-notched laser powder bed fused AlSi10Mg samples and the experimental data were further analyzed with ML approaches, to identify the correlation between residual stress, hardness and surface roughness, to improve the prediction of the fatigue life of such specimens. According to this analysis, the number

of research focusing on the use of ML algorithms for the prediction of the fatigue response of AM parts has increased in the last years, highlighting the capability of ML algorithms of managing multivariate problems concerning the structural integrity of AM parts. In the present paper, physics informed ML algorithms have been developed to predict the stress-life relationship of Ti6Al4V specimens produced through an SLM process. The algorithms proposed in this paper have been trained with a direct approach with no intermediate NN, on a fully populated training database with a high numerosity (768 fatigue points in the TDB with 76 datasets collected in the literature). Several other peculiarities will be discussed in the following pages.

## 2 | MACHINE LEARNING ALGORITHMS

In this section, the developed ML algorithms are described. Section 2.1 focuses on the process parameters considered as the input of the developed ML algorithms. Section 2.2 reports details on the training database and how it has been built. Section 2.3 focuses on the preliminary tuning of the Feed Forward NN (FFNN) algorithm, analyzing also the importance of the feature numerical correlation. In order to avoid non-feasible S-N curves, Section 2.4 explores the capabilities of the PINN algorithm. Finally, a bi-linear FFNN is developed in Section 2.5, providing the best predictions.

### 2.1 | Input variables: process parameters and post-treatments

This section focuses on the process parameters which have been considered as the input for the developed NN algorithms. The objective of the proposed ML algorithm is the prediction of the fatigue life and, accordingly, of the S-N curves of SLM Ti6Al4V parts starting from the process parameters. This approach would facilitate the assessment of the allowable stress to be considered for the design against fatigue failures of SLM Ti6Al4V parts, since the fatigue response of this alloy is strongly dependent on the defect population. In order to improve the predictive capability, post-treatments have been also considered, as detailed in the following. The input of the NN should be carefully chosen, to properly predict the fatigue response. During the SLM process, the laser hits the powders laid on the SLM machine bed, melting them and solidifying gradually the first layer. Each layer has a thickness and this can be set according to the parameter named “layer thickness”  $t$  [ $\mu\text{m}$ ], which is the distance

that the plate of the building chamber will travel downward to let the blade recoat a new layer of powder. The laser passes again, completing another layer and the process is repeated several times until the part is completed. This occurs in a chamber that has a protected atmosphere with inert gases, to avoid any type of unwanted chemical bond. The orientation of the part on the building platform is also an important factor affecting the resulting mechanical performance.<sup>7</sup> Generally, three configurations identifying the building orientation  $\vartheta$ , that is, the angle between the part and the building platform, are employed in the industrial practice: horizontal ( $0^\circ$ ), vertical ( $90^\circ$ ), and inclined ( $45^\circ$ ). This process parameter significantly influences the defect population and the subsequent fatigue life.<sup>7</sup> The hatch distance  $h$  [ $\mu\text{m}$ ], corresponding to the distance between one laser pass and the next one, has to be carefully chosen. If  $h$  is too high, it means that two subsequent passages may lead to partially melted particles. Too small hatch distances, on the other hand, increase the production time, with multiple remelting of the same section of layer.<sup>36</sup> The laser power  $P$  [W] and the laser scan speed  $v$  [mm/s] are also among the most influencing parameters. The first one dictates how much power the laser is providing to the powders, while the latter one determines how quickly the laser passes to create the layer of material. If the speed is too high and the power is too small, the powder does not have enough time to melt. On the contrary, too large power and small scan speed, may lead to multiple remelting of the previous layers, affecting the quality of the finished part.<sup>37</sup> The above analysis highlights how crucial process parameter tuning is.<sup>5</sup> Other parameters are often cited in the literature and set before the manufacturing process (point distance [ $\mu\text{m}$ ], exposure time [ $\mu\text{s}$ ], plate temperature [ $^\circ\text{C}$ ], powder size [ $\mu\text{m}$ ], scanning strategy [ $^\circ$ ], beam diameter [ $\mu\text{m}$ ], and powder size [ $\mu\text{m}$ ]). However, these parameters are generally missing in literature papers, due to their small influences, and are not considered as input parameters for the developed NN, as this won't lead to obtain a fully populated TDB. Thermal treatments as annealing or HIP are also largely employed<sup>9</sup> and significantly affect the fatigue response. Since the powder is fused at high temperatures, with a rapid subsequent decrement, the final part can undergo distortions and residual stresses. The gradual solidification of each layer creates high thermal stresses that affect both the mechanical properties and the shape of the component. To counteract this issue, annealing thermal treatments are generally employed, with the component reheated in a furnace at a temperature ( $500^\circ\text{C}$  to  $950^\circ\text{C}$ ) significantly below the melting point ( $1660^\circ\text{C}$ ) for enough time (30 min to 4 h). On the other hand, the HIP thermal treatment has proven<sup>22</sup> to remarkably increase the

fatigue life of Ti6Al4V parts by reducing the size of porosities and defects. In the HIP process, high pressures (1000 to 2000 bar) and high temperatures (800°C to 1050°C) are simultaneously applied to the specimens, for a couple of hours (2 to 3 h), in a specifically designed chamber filled with inert gas, allowing to close defects and porosities. Accordingly, the thermal and the HIP treatments have been considered as the inputs of the developed ML algorithms. The specimen surface and, in particular, surface defects have a significant influence on the fatigue response. In general, AF parts tend to have a poor surface finish, with consequent low fatigue performances. To enhance the surface quality, one or more surface treatments are used, like LSP,<sup>11</sup> SP,<sup>12,13</sup> polishing, surface machining, SMAT,<sup>14</sup> Electric Discharge Machining (EDM),<sup>19</sup> surface machining, and SB.<sup>15</sup> This is the reason why even surface treatments have been considered as the input of the NN.

## 2.2 | Training database: Features and labels

The creation of a fully populated TDB is fundamental to obtain reliable predictions with ML algorithms. The database must have as much data as possible and the input features  $x_i$  must be strongly correlated to the variables to be predicted (the fatigue life  $N_f$  in this application). In ML literature, the input variables are called features ( $x_i$ ), while the variables to be predicted are named labels ( $y_i$ ). In this work, the datasets have been collected from the SLM Ti6Al4V fatigue literature. According to Section 2.1, only those reporting the  $P$ ,  $v$ ,  $t$ ,  $h$  and  $\vartheta$  values as process parameters, information on the thermal and surface treatments and, for each failure, the stress amplitude, and the corresponding number of cycles to failure have been considered. In particular, the experimental data have been digitized from the S-N plots reported in the investigated literature papers by using the software “Engauge Digitizer.” Literature fatigue tests are carried out in different configurations, mainly rotating bending ( $R = \sigma_{min}/\sigma_{max} = -1$ , being  $R$  the stress ratio,  $\sigma_{min}$  and  $\sigma_{max}$  the minimum and the maximum stress within a load cycle, respectively) and pulsating tensile ( $R > 0$ ,  $\sigma_{max} > 0$ ,  $\sigma_{min} > 0$ ,  $\sigma_m > 0$ ). In order to consider together all the data, the Smith-Watson-Topper correction was applied by calculating the equivalent stress amplitude,  $\sigma_{a,R=-1}$ , at  $R = -1$  ( $\sigma_{a,R=-1} = \sigma_{max} \cdot \sqrt{0.5 \cdot (1-R)}$ ). The database has been built to be fed inside the Python programming environment and to be read, as a CSV file, by the Python library named “pandas.” Therefore, it will have as many rows as the number of fatigue points that have been digitized from the articles, and as many

columns as the features that are used to predict  $N_f$ . It is of fundamental importance to avoid blank spots in the database, to let the ML algorithm work properly. To denote whether the annealing and HIPing treatments have been performed, a Boolean strategy has been adopted, that is, equal to 1 if applied and to 0 if not applied. For the thermal treatments, as it was anticipated before, the presence of the annealing and HIP treatments were noted in the TDB, as well as the annealing temperature (if the annealing was not performed,  $T$  was reported as 20°C). While for the surface treatments, again a Boolean strategy was chosen to discriminate whether the treatment has been applied or not. The surface treatments which have been considered are the following, according to Section 2.1: machining, SB, SP, LSP, SMAT, EDM, and surface polishing. Together with the process parameters and the surface treatments, the stress amplitude  $\sigma_a$  was used as a feature to predict the label fatigue life  $N_f$ . This was done to replicate what occurs in fatigue testing: indeed, before a test, the stress amplitude  $\sigma_a$  is fixed, and the number of cycles to failure is experimentally assessed. The opposite strategy, that is, considering  $N_f$  as the input feature and  $\sigma_a$  as the predicted value, could have been used anyways and it is expected that the results would not have varied significantly. In the investigated datasets, runout data are also present. However, they have not been considered in the developed algorithms, since they require the application of appropriate statistical methodologies which can add further complexities to the models and are out of the scope of the present work. Table 1 summarizes the data used for validating the developed ML algorithms. In total, 768 fatigue points have been considered in the present work. Those ones are coming from 76 datasets extrapolated from 18 articles (Table 1). The amount of data for each literature dataset varies significantly, with datasets having only one point per stress amplitude level. These datasets have not been discarded since other datasets, obtained with similar process parameters, increased the number of points having the same stress amplitude level.

In the considered articles, experimental tests have been mainly carried out on specimens characterized by standard geometries for rotating bending and pulsating tensile tests. However, the specimen geometry or the specimen risk-volume can significantly affect the fatigue response. These two factors have not been considered in the ML algorithms, since standard geometries have been mainly tested, therefore not significantly affecting the fatigue response, even if contributing to the large experimental scatter. It must be noted that a proper strategy for optimizing the predicting capabilities of ML algorithms is to start predicting the label with a small number of features and, thereafter, increase the number to improve the accuracy of the predictions. For example, in the first

**TABLE 1** The structure of the training database, each row corresponds to a different dataset. Each fatigue point corresponding to the same dataset shares the same parameters and treatment but has a different  $\sigma_e$  and  $N_f$ .

Code	Article	Name	$\phi$	P	h	v	t	Ann	T	HIP	Mac	SB	EDM	LSP	SP	SMAT	Pol
0	DuQian2020 <sup>5</sup>	1	90	120	0.07	1200	30	1	600	0	0	0	0	0	0	0	1
1	DuQian2020 <sup>5</sup>	2	90	120	0.1	1000	45	1	600	0	0	0	0	0	0	0	1
2	DuQian2020 <sup>5</sup>	3	90	120	0.13	800	60	1	600	0	0	0	0	0	0	0	1
3	DuQian2020 <sup>5</sup>	4	90	160	0.13	1000	30	1	600	0	0	0	0	0	0	0	1
4	DuQian2020 <sup>5</sup>	5	90	160	0.07	800	45	1	600	0	0	0	0	0	0	0	1
5	DuQian2020 <sup>5</sup>	6	90	160	0.1	1200	60	1	600	0	0	0	0	0	0	0	1
6	DuQian2020 <sup>5</sup>	7	90	200	0.1	800	30	1	600	0	0	0	0	0	0	0	1
7	DuQian2020 <sup>5</sup>	8	90	200	0.13	1200	45	1	600	0	0	0	0	0	0	0	1
8	DuQian2020 <sup>5</sup>	9	90	200	0.07	1000	60	1	600	0	0	0	0	0	0	0	1
9	DuQian2020 <sup>5</sup>	10	90	160	0.07	1000	30	1	600	0	0	0	0	0	0	0	1
10	Gunther2017 <sup>6</sup>	SLM-1a	90	175	0.12	710	30	1	800	0	1	0	0	0	0	0	0
11	Gunther2017 <sup>6</sup>	SLM-1b	90	175	0.12	710	30	1	800	0	1	0	0	0	0	0	1
12	Gunther2017 <sup>6</sup>	SLM-2	90	175	0.12	710	30	1	800	1	1	0	0	0	0	0	1
13	Hu2020 <sup>38</sup>	noName	90	280	0.14	1200	30	1	500	0	0	0	0	0	0	0	1
14	Li2016 <sup>19</sup>	Edwards & Ramulu As Built	0	200	0.18	200	50	0	20	0	0	0	0	0	0	0	0
15	Li2016 <sup>19</sup>	Edwards & Ramulu Machined and Polished	0	200	0.18	200	50	0	20	0	1	0	0	0	0	0	1
16	Li2016 <sup>19</sup>	Xu et al. Annealed	90	375	0.12	1029	60	1	640	0	1	0	0	0	0	0	0
17	Li2016 <sup>19</sup>	Xu et al. AB 0°	0	375	0.12	1029	60	0	20	0	1	0	0	0	0	0	0
18	Li2016 <sup>19</sup>	Xu et al. AB 90°	90	375	0.12	1029	60	0	20	0x	1	0	0	0	0	0	0
19	Li2016 <sup>19</sup>	Hoerweder et al.	90	250	0.06	1600	30	1	650	0	0	0	1	0	0	0	0
20	Li2016 <sup>19</sup>	Kasperovich & Hausmann Machined and Polished	90	200	0.25	1250	40	0	20	1	1	0	0	0	0	0	0
21	Li2016 <sup>19</sup>	Kasperovich & Hausmann AB	90	200	0.25	1250	40	0	20	1	0	0	0	0	0	0	0
22	Sanaei2020 <sup>8</sup>	AM250 Annealed	90	400	0.16	1000	50	1	700	0	0	0	0	0	0	0	0
23	Sanaei2020 <sup>8</sup>	AM250 AB	90	400	0.16	1000	50	0	20	1	0	0	0	0	0	0	0
24	Sanaei2020 <sup>8</sup>	AM250 Annealed and Machined	90	400	0.16	1000	50	1	700	0	1	0	0	0	0	0	0
25	Sanaei2020 <sup>8</sup>	M290 90° Annealed	90	285	0.14	1200	30	1	700	0	1	0	0	0	0	0	0
26	Sanaei2020 <sup>8</sup>	M290 45° Annealed	45	285	0.14	1200	30	1	700	0	1	0	0	0	0	0	0
27	Sanaei2020 <sup>8</sup>	M290 90° AB	90	285	0.14	1200	30	0	20	1	1	0	0	0	0	0	0

TABLE 1 (Continued)

Code	Article	Name	$\phi$	$P$	$h$	$v$	$t$	Ann	$T$	HIP	Mac	SB	EDM	LSP	SP	SMAT	Pol
28	Sanaei2020 <sup>8</sup>	M290 45° AB	45	285	0.14	1200	30	0	20	1	1	0	0	0	0	0	0
29	Zhao2016 <sup>20</sup>	SLM-V7	90	200	0.1	1000	50	0	20	0	1	0	0	0	0	0	0
30	Zhao2016 <sup>20</sup>	H-SLM-V7	90	200	0.1	1000	50	0	20	1	1	0	0	0	0	0	0
31	Fousova2018 <sup>21</sup>	SLM	90	200	0.08	1250	30	1	820	0	0	0	0	0	0	0	0
32	Jiang2021 <sup>11</sup>	HT	0	190	0.065	1000	30	1	955	0	0	0	0	0	0	0	1
33	Jiang2021 <sup>11</sup>	LSP2	0	190	0.065	1000	30	0	20	0	0	0	0	1	0	0	1
34	Sun2021 <sup>22</sup>	Ultrasonic	90	360	0.1	1200	60	1	710	1	0	0	0	0	0	0	1
35	Sun2021 <sup>22</sup>	Rotating bending	90	360	0.1	1200	60	1	710	1	0	0	0	0	0	0	1
36	Gunther2018 <sup>16</sup>	Batch 1-1	90	175	0.12	710	30	1	800	0	1	0	0	0	0	0	0
37	Gunther2018 <sup>16</sup>	Batch 1-2	90	175	0.12	710	30	1	800	0	1	0	0	0	0	0	0
38	Gunther2018 <sup>16</sup>	Batch 1-3	90	175	0.12	710	30	1	800	0	1	0	0	0	0	0	0
39	Gunther2018 <sup>16</sup>	Batch 2	90	175	0.12	710	30	1	800	0	1	0	0	0	0	0	0
40	Gunther2018 <sup>16</sup>	Batch 3	90	175	0.12	710	30	1	800	0	1	0	0	0	0	0	0
41	Eric2016 <sup>12</sup>	As Built	45	170	0.1	1250	30	1	650	0	0	0	0	0	0	0	0
42	Eric2016 <sup>12</sup>	Polished	45	170	0.1	1250	30	1	650	0	0	0	0	0	0	0	1
43	Eric2016 <sup>12</sup>	Shot Peened	45	170	0.1	1250	30	1	650	0	0	0	0	0	1	0	0
44	Gong2015 <sup>15</sup>	SLM-OP 1	90	120	0.1	960	30	0	20	0	1	1	0	0	0	0	1
45	Gong2015 <sup>15</sup>	SLM-MP 2	90	120	0.1	540	30	0	20	0	1	1	0	0	0	0	1
46	Gong2015 <sup>15</sup>	SLM-MP 3	90	120	0.1	400	30	0	20	0	1	1	0	0	0	0	1
47	Gong2015 <sup>15</sup>	SLM-MP 4	90	120	0.1	1260	30	0	20	0	1	1	0	0	0	0	1
48	Gong2015 <sup>15</sup>	SLM-MP 5	90	120	0.1	1500	30	0	20	0	1	1	0	0	0	0	1
49	Alegre2022 <sup>9</sup>	As Built	90	400	0.12	150	60	0	20	0	1	0	0	0	0	0	0
50	Alegre2022 <sup>9</sup>	HIP	90	400	0.12	150	60	0	20	1	1	0	0	0	0	0	0
51	Macallister2022 <sup>17</sup>	AF test	90	170	0.1	1200	30	0	20	0	0	0	0	0	0	0	0
52	Mertova2018 <sup>10</sup>	AH	90	200	0.08	1250	30	0	20	1	0	0	0	0	0	0	0
53	Mertova2018 <sup>10</sup>	MH	90	200	0.08	1250	30	0	20	1	1	0	0	0	0	0	1
54	Mertova2018 <sup>10</sup>	M	90	200	0.08	1250	30	1	820	0	1	0	0	0	0	0	1
55	Tehrani2021 <sup>18</sup>	AB Coarse East	90	280	0.14	1200	30	1	900	0	0	0	0	0	0	0	0
56	Tehrani2021 <sup>18</sup>	AB Fine East	90	280	0.14	1200	30	1	900	0	0	0	0	0	0	0	0
57	Tehrani2021 <sup>18</sup>	M Coarse East	90	280	0.14	1200	30	1	900	0	1	0	0	0	0	0	1

(Continues)

TABLE 1 (Continued)

Code	Article	Name	$\phi$	P	h	v	t	Ann	T	HIP	Mac	SB	EDM	LSP	SP	SMAT	Pol
58	Tehrani2021 <sup>18</sup>	M Coarse West	90	280	0.14	1200	30	1	900	0	1	0	0	0	0	0	1
59	Tehrani2021 <sup>18</sup>	M Fine East	90	280	0.14	1200	30	1	900	0	1	0	0	0	0	0	1
60	Tehrani2021 <sup>18</sup>	M Fine West	90	280	0.14	1200	30	1	900	0	1	0	0	0	0	0	1
61	Yan2019 <sup>14</sup>	AF	90	280	0.05	1200	30	0	20	0	0	0	0	0	0	0	0
62	Yan2019 <sup>14</sup>	HIP	90	280	0.05	1200	30	0	20	1	1	0	0	0	0	0	0
63	Yan2019 <sup>14</sup>	SMAT	90	280	0.05	1200	30	0	20	1	1	0	0	0	0	1	0
64	Kumar2020 <sup>13</sup>	3090-AF	90	280	0.14	1200	30	0	20	0	1	0	0	0	0	0	1
65	Kumar2020 <sup>13</sup>	3090-HT	90	280	0.14	1200	30	1	920	0	1	0	0	0	0	0	1
66	Kumar2020 <sup>13</sup>	3090-SP	90	280	0.14	1200	30	1	920	0	1	0	0	0	1	0	0
67	Kumar2020 <sup>13</sup>	3067-AF	90	280	0.14	1200	30	0	20	0	1	0	0	0	0	0	1
68	Kumar2020 <sup>13</sup>	3067-HT	90	280	0.14	1200	30	1	920	0	1	0	0	0	0	0	1
69	Kumar2020 <sup>13</sup>	3067-SP	90	280	0.14	1200	30	1	920	0	1	0	0	0	1	0	0
70	Kumar2020 <sup>13</sup>	6090-AF	90	340	0.12	1250	60	0	20	0	1	0	0	0	0	0	1
71	Kumar2020 <sup>13</sup>	6090-HT	90	340	0.12	1250	60	1	920	0	1	0	0	0	0	0	1
72	Kumar2020 <sup>13</sup>	6090-SP	90	340	0.12	1250	60	1	920	0	1	0	0	0	1	0	0
73	Kumar2020 <sup>13</sup>	6067-AF	90	340	0.12	1250	60	0	20	0	1	0	0	0	0	0	1
74	Kumar2020 <sup>13</sup>	6067-HT	90	340	0.12	1250	60	1	920	0	1	0	0	0	0	0	1
75	Kumar2020 <sup>13</sup>	6067-SP	90	340	0.12	1250	60	1	920	0	1	0	0	0	1	0	0



FFNN (Section 2.3), only the process parameters ( $\vartheta$ ,  $t$ ,  $h$ ,  $P$ , and  $v$ ) and the stress amplitude ( $\sigma_a$ ), have been used. The heat and surface treatments were gradually added to verify the improvement of the predictive power. Finally, it was observed that a feature cross combination (combination of two or more features via multiplication or division) between  $P$  and  $v$ , significantly improved the quality of the predictions. This idea originated from the well-known relation that lies between those two parameters<sup>37</sup> and confirmed to be correct because the correlation vector referred to  $N_f$ , with the  $v/P$  feature cross combination, gave a higher coefficient with respect to  $v$  and  $P$  considered alone. This improved the predictions significantly.

## 2.3 | Feed forward neural network

The FFNN is the simplest model of neural network, in which data can propagate only in the forward direction, so from the input layer to the output layer, as there is no information traveling backwards. The structure of the neural network should be properly designed to result in optimized predictions. The input layer takes the signal moving it to the next hidden layer, and so on up to the final output layer. Inside the hidden layers the neurons work together by taking the signal from the inputs and by producing a random weight ( $w_i$ ) and a bias ( $b_i$ ) that are combined with the input features ( $x_i$ ) to produce a sum ( $g_i$ ), calculated as follows (Equation (1)):

$$g_i = w_i \cdot x_i + b_i. \quad (1)$$

The sum  $g_i$  is fed through the activation function ( $f_{a,i}$ ), arbitrarily chosen for each dense layer, that changes the signal by activating it. The activation function can be a sigmoid, a linear, a rectified linear unit (ReLU) or a hyperbolic tangent (tanh) function. The activated signal is sent to the next layers up until the output one, delivering the prediction for the current training repetition (epoch). The output layer is linearly activated as the other types of  $f_{a,i}$  would act as a filter, distorting the final information (Equation (2)):

$$y_i = f_{a,i}(g_i). \quad (2)$$

A fundamental ML hyper-parameter is the number of epochs. The process that has been stated few lines before is repeated as many times as the number of epochs and, as this process repeats, all the weights and the biases are adjusted at each epoch to increase the quality of the prediction. The metric that measures how precise the prediction is, is named **loss function**. Generally, it is used the

loss function that minimizes the mean squared error (MSE). When the MSE is calculated, the weights and biases are adjusted again to ensure that the MSE is reduced in the next epoch. The learning rate (LR) is the 2nd fundamental ML hyper-parameter. It tells the neural network how much to modify the biases and weights in response to the previously calculated loss. Tuning the LR correctly is important as the loss of the model could even increase if the LR is set high or decrease very slowly if set low, requiring then more training epochs and time. Lastly, the batch size indicates the number of rows of the TDB passed through to the NN at one time. It can range from 1 to the size of the full database. Both extreme values deteriorate the prediction. A good compromise is a value in between: for this work the batch size has been set to 500. For how important the hyper-parameters tuning is, what really determines the goodness of the NN is the correctness and coherence of the TDB. Therefore, as a starting point, a simplified version of the training database is firstly considered with only  $P$ ,  $v$ ,  $t$ ,  $h$ ,  $\vartheta$ , and  $\sigma_a$  as input features (Figure 1, light blue). This has allowed to verify the capability of the proposed ML for dealing with the fatigue response of Ti6Al4V parts. In a later stage of the FFNN, all the thermal and surface treatments (Figure 1, dark blue) have been considered during the training to improve the precision. In Figure 1 it is possible to appreciate the structure for this first NN. It is composed of 16 input nodes (6 light blue and 10 dark blue, one per feature), 3 intermediate hidden layers with respectively 100, 75, and 50 neurons (green) having the ReLU as activation function, and 1 linearly activated output node for  $N_f$  (red). The hidden part can be arbitrarily set to enhance the precision of the training process. After extensive testing, the ML hyper-parameters are set as follows: epochs = 300 to 500, learning rate = 0.001 and the batch size = 500. The TDB is normalized ( $TDB_{norm}$ ), following the z-score column-wise formula ( $TDB_{norm} = [TDB - TDB_{mean}] / TDB_{stdev}$ , being  $TDB_{mean}$  the TDB mean and  $TDB_{stdev}$  the TDB standard deviation).

Once the NN has been trained, the prediction accuracy has been verified on a randomly dataset chosen. To this end, the dataset *Gong2015 SLM-MP 4*<sup>15</sup> has been selected. An evaluation database has been built to interrogate the part of the FFNN that has the same process parameters of the chosen dataset. Those ones are repeated identically through each row while the  $\sigma_a$  column varies between the minimum and the maximum  $\sigma_a$  of the dataset with 1 MPa increments. This evaluation database has been normalized again with the z-score to be fed inside the FFNN to output the normalized  $N_f$  prediction. After de-normalizing the predicted life with the inverse formula of the z-score, this one is plotted with  $\sigma_a$  on top

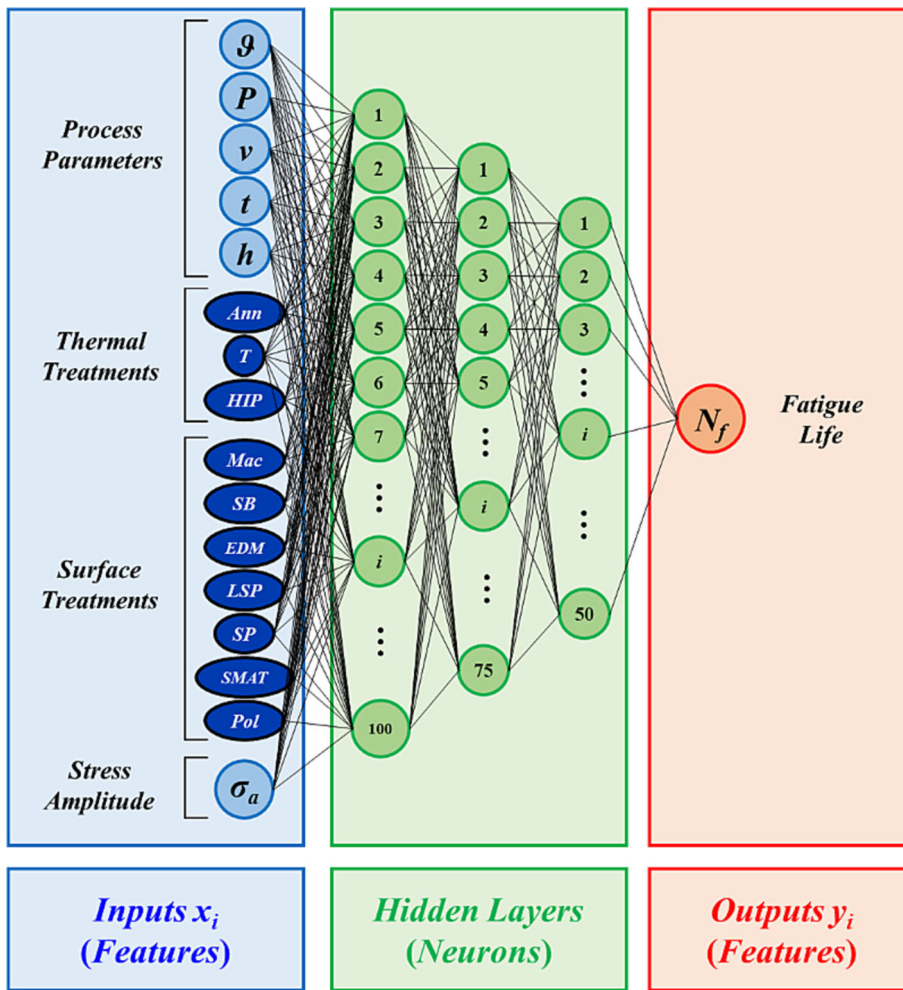


**FIGURE 1** The structure of the Feed Forward NN (FFNN). In blue is represented the input layer, whose nodes are as many as the features  $x_i$  that are used to predict the variable of interest. In green are shown the intermediate layers with their neurons, which can be customized at will to meet an efficient and precise training. In red is depicted the output layer, in which each node corresponds to the label  $y_i$  to be predicted. [Colour figure can be viewed at [wileyonlinelibrary.com](https://onlinelibrary.wiley.com/doi/10.1111/ffe.14254)]

	$\vartheta$	$h$	$t$	$P$	$v$	$P/v$	$P \cdot v$	$v/P$
$N_f$ [%]	14.63	18.93	8.10	9.50	6.77	9.62	1.19	13.54

**TABLE 2**  $N_f$  feature correlation vector of the process parameters with all the possible feature crosses between  $v$  and  $P$ .

of the experimental points of the dataset to reveal the predicted fatigue curve.

### 2.3.1 | Correlation coefficients

Before implementing important modifications, it is good practice to study the correlation between the features toward that label  $N_f$ . With this, it is possible to verify which feature has high predictive power. Table 2 shows the  $N_f$  correlation vector: the first 5 columns display the correlation coefficients of  $P$  and  $v$  and the three other process parameters alone, while in the last three all the possible feature cross combinations between  $P$  and  $v$  have been reported with their correlation coefficients. It can be observed that  $P$  and  $v$  alone have a low correlation coefficient toward fatigue life. It is also known that they

are physically related to each other, as discussed in Section 2.2. Therefore, a feature cross combination has been considered between these two parameters. Three attempts have been made:  $P/v$ ,  $P \cdot v$  and  $v/P$ ; with  $v/P$  providing the highest correlation coefficient. In the final configuration of the TDB, the  $h$ ,  $\vartheta$  and  $t$  correlation coefficients remained unchanged while the feature cross  $v/P$  replaced the process parameters  $v$  and  $P$ , thanks to its higher predictive power.

## 2.4 | The physics informed neural network

The first developed NN works as a “black box” not ensuring that the fatigue life decreases with the applied number of cycles. Accordingly, this physical evidence can be

embedded in the NN. With this information embedded, a physics informed neural network (PINN<sup>39</sup>) is created. As the model trains, through each epoch, for each considered dataset, all the experimental data points are considered and the 1st derivative is computed. In particular, since the model predicts  $N_f$ , the 1st derivative is defined as  $dN_f / d\sigma_a$ . The first derivative,  $dN_f / d\sigma_a$ , has been imposed to be negative within an appropriate custom loss function, reported in Equation (3):

$$\text{totalLoss} = a \cdot f + b \cdot \text{MSE}, \quad (3)$$

being  $f$  a custom penalization function which has been defined such that the negative derivatives are not making the loss increase, since they are zeroed, while positive derivatives worsen the training loss. The  $a$  and  $b$  coefficients, whose sum must be equal to 1, are used to give a weight to the terms associated to the derivative ( $f$ ) and the mean square error function, respectively. The  $f$  function is defined according to Equation (4):

$$f = \frac{\frac{dN_f}{d\sigma_a} + \left| \frac{dN_f}{d\sigma_a} \right|}{2}. \quad (4)$$

Figure 2 plots the  $f$  function (in blue) for a sinusoidal  $dN_f/d\sigma_a$  function (in dotted red).

This ensures that the S-N curves are always decreasing. The  $a$  and  $b$  coefficients have both been set to 0.5 to give an equal weight to both the MSE term and the derivative term. Equation 5 reports the trivial constraints of the  $a$  and  $b$  coefficients:

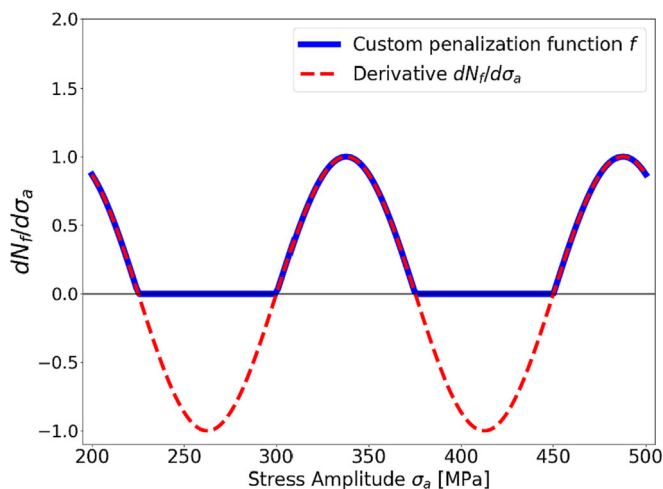


FIGURE 2 Custom penalization function  $f$  (blue) used to penalize positive derivatives and to inject the physics of fatigue problems inside the Physics Informed Neural Network (PINN). [Colour figure can be viewed at [wileyonlinelibrary.com](http://wileyonlinelibrary.com)]

$$a + b = 1, \quad (5)$$

For each dataset the training was repeated 5 times to get an average and mitigate the randomness that is present while training a NN, ensuring the best performances. The structure of the NN remains identical, though the tanh activation function has been implemented in all the hidden layers.

## 2.5 | Bi-linear neural network

Finally, the estimated S-N curves are forced to follow a bilinear trend, according to the experimental evidence. In the following, the developed NN will be called Bi-Linear Feed-Forward Neural Network (BLFFNN). The TDB has been reshaped, since the output labels of the BLFFNN are now the four coefficients of the bilinear model, the slopes  $m_1$  and  $m_2$  and the biases  $q_1$  and  $q_2$  according to Equation (6):

$$\begin{cases} S = m_1 \cdot N + q_1, & \text{if } S \leq S_* \\ S = m_2 \cdot N + q_2, & \text{if } S > S_* \end{cases} \quad (6)$$

The features are the same as before with the exception that the feature cross  $v/P$  is now being replaced back by  $P$  and  $v$  alone as for the FFNN, since the TDB is different. The input layer is the same of the preliminary FFNN with the  $\sigma_a$  feature node excluded. The hidden part of the BLFFNN is identical to the PINN, while the output layer has now 4 nodes, accordingly one per label.

In this configuration, for each dataset the coefficients of the bilinear model fitting the experimental data need to be estimated, according to Figure 3. The line fitting the experimental data failing at small number of cycles (typically in the Low Cycle Fatigue (LCF)–High Cycle Fatigue (HCF) life region) crosses point A, (Figure 3), whereas the line fitting failures at large number of cycles (typically in the Very High Cycle Fatigue [VHCF] life region) crosses the point B in Figure 3.

Both points A and B have been chosen from the top left region and the bottom right region of the considered dataset experimental S-N diagram. Accordingly, only the slopes  $m_1$  and  $m_2$  are to be estimated. In particular, the slopes ensuring the lowest RMSE( $N_f$ ), hence those providing the best fitting of the data, have been considered. To force the concavity to be facing upward, an  $m^*$  slope coefficient has been considered as upper limit for the  $m_1$  slope vector and as lower limit for the  $m_2$  vector.  $m^*$  is simply the slope coefficient of the line passing through points A and B. This forced the knee point (Point \*, Figure 3) to stay below the line passing through points A

and B (Line \*, Figure 3). Accordingly, it can be ensured that the knee point and the bilinear function are enclosed in the right triangle identified by points A and B. This allows the network to follow the typical experimental trend, without the need for a PINN that increases the computation time and the network complexity. This procedure is repeated for all 76 datasets until the TDB is fully populated.

### 3 | RESULTS AND DISCUSSION

In this section the three developed ML algorithms are validated on literature data. In Section 3.1, the preliminary results of the FFNN are shown. Those are useful to

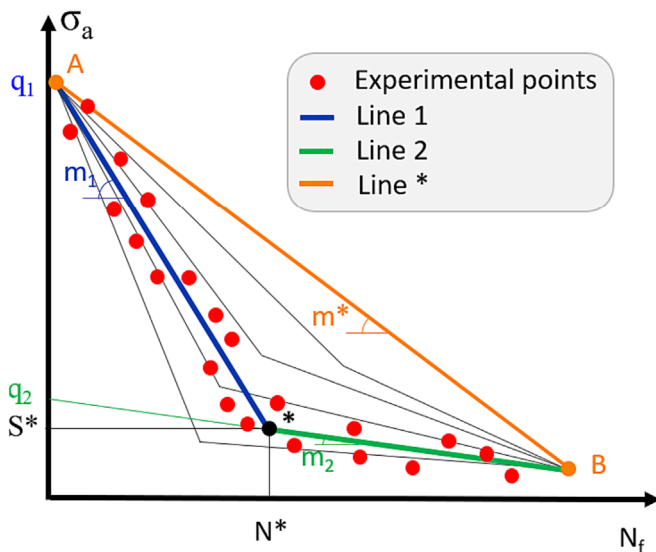


FIGURE 3 Schematic stress-life diagram showing the strategy followed to fit the experimental data with a bilinear trend. [Colour figure can be viewed at [wileyonlinelibrary.com](https://onlinelibrary.wiley.com/doi/10.1111/ffe.1425)]

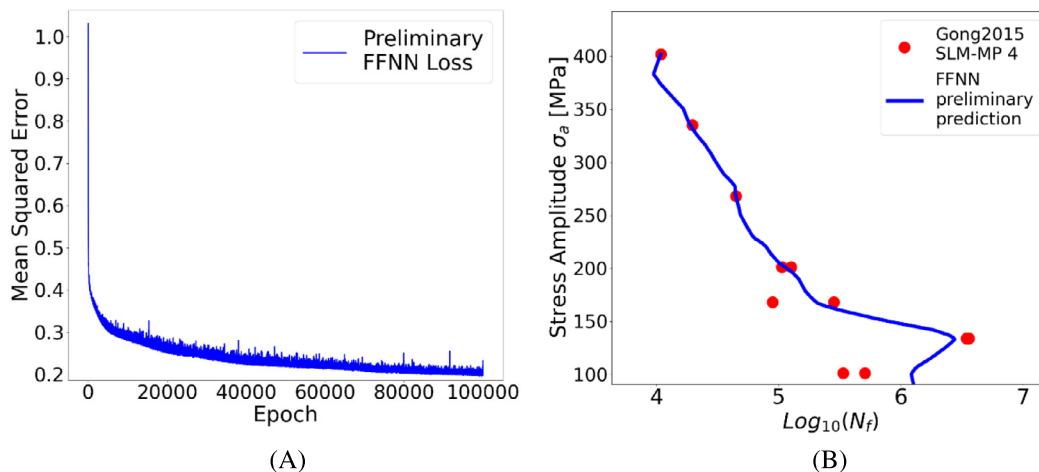


FIGURE 4 (A) The preliminary Feed Forward NN (FFNN) model loss to validate the chosen set of hyper-parameters. The first raw preliminary prediction of the FFNN is revealed in (B). [Colour figure can be viewed at [wileyonlinelibrary.com](https://onlinelibrary.wiley.com/doi/10.1111/ffe.1425)]

understand the right direction to take when it comes to implementing further improvements. In Section 3.2, the improvement of the S-N curves is evidenced by the analysis of the figures obtained from the PINN algorithm. Section 3.3 shows the obtainment of the desirable bilinear behavior, that is representative of the experimental evidence of fatigue curves. In Section 3.4, the three NN types are compared to highlight which of them performs best. Section 3.5 reports the validation on test datasets accomplished by removing those sets from the training database; this has been done to show the limits of each neural network type. Section 3.6 outlines another validation achieved by using new datasets that are out of the TDB, therefore the network is predicting the life blindly from the process parameters and treatments of the sets to be validated. Lastly, Section 3.7 shows the influence of the process parameters variation on the fatigue life of the specimens.

#### 3.1 | FFNN validation

The model trained from normalized data showed a step training loss decrease in the first 200 epochs as it reaches an MSE value of 0.3. To be conservative, the number of epochs has been increased to 100,000. Figure 4A plots the loss function with respect to the number of epochs. According to Figure 4, an overall flat trend of the training loss has been obtained. The training can be stopped at 500 epochs to reach a satisfactory performance. If more than 1000 epochs are used, an undesired overfitting behavior is obtained, with an unnecessarily increased training time. In Figure 4B the first preliminary S-N curve prediction has been performed on the randomly chosen dataset “Gong 2015 SLM-MP 4.”<sup>15</sup>

According to the preliminary investigation in Figure 4B, it can be stated that the predicted S-N curve is close to the experimental data. However, this result has three main issues: it has not a strictly decreasing behavior, the concavity is not always facing upward and the shape is not typical of fatigue problems, as many broken lines are present. Even considering in the TDB the heat and surface treatments, these three problems remained unsolved. The “black box” approach, accordingly, should be considered as a starting point and prove the effectiveness of the methodology, since the S-N curve estimated from the process parameters, heat and surface treatments is close to the experimental data, but it cannot be used for the design of components due to the above-mentioned issues.

### 3.2 | PINN curves

Once the PINN algorithm has been created, its predicting capabilities can be evaluated by considering all 76 datasets. Figure 5 shows 6 datasets evaluated with the PINN algorithm: in black 5 fatigue curves predicted by the PINN while in orange the average of those 5 S-N curves.

This 5-curves mean has been produced to reduce the randomness of the training sessions. Figure 5A shows the dataset “Gong 2015 SLM-MP 4”<sup>15</sup> evaluated with the PINN algorithm; with respect to Figure 4B the quality has improved significantly as the behavior is smoother and strictly decreasing. The same holds for Figure 5B,C representing the datasets “DuQian2020, set 1”<sup>5</sup> and “Alegre2022 as built”<sup>9</sup> respectively. Figure 5D depicts set “Li2016, Hooerweder et al.”<sup>19</sup> Linear trends are also achieved by the PINN, as it is observable in Figure 5E,F showing the datasets “Gunther2017, SLM-1 b”<sup>6</sup> and “Kumar2020 3067-AF.”<sup>13</sup> According to Figure 5A,B,D-F, very good predictions can be obtained, with the predicted S-N curves crossing the experimental data and, at the same time, being strictly decreasing, with a smooth trend and the concavity facing upward. This has been found for nearly 75% of the datasets. On the other hand, P-S-N curves with the concavity facing downward are still found, and an example can be appreciated in Figure 5C. Accordingly, the PINN algorithm provides good results and works properly for the majority of the considered datasets, but not feasible S-N curves with trends in contrast with the experimental trend can be still found.

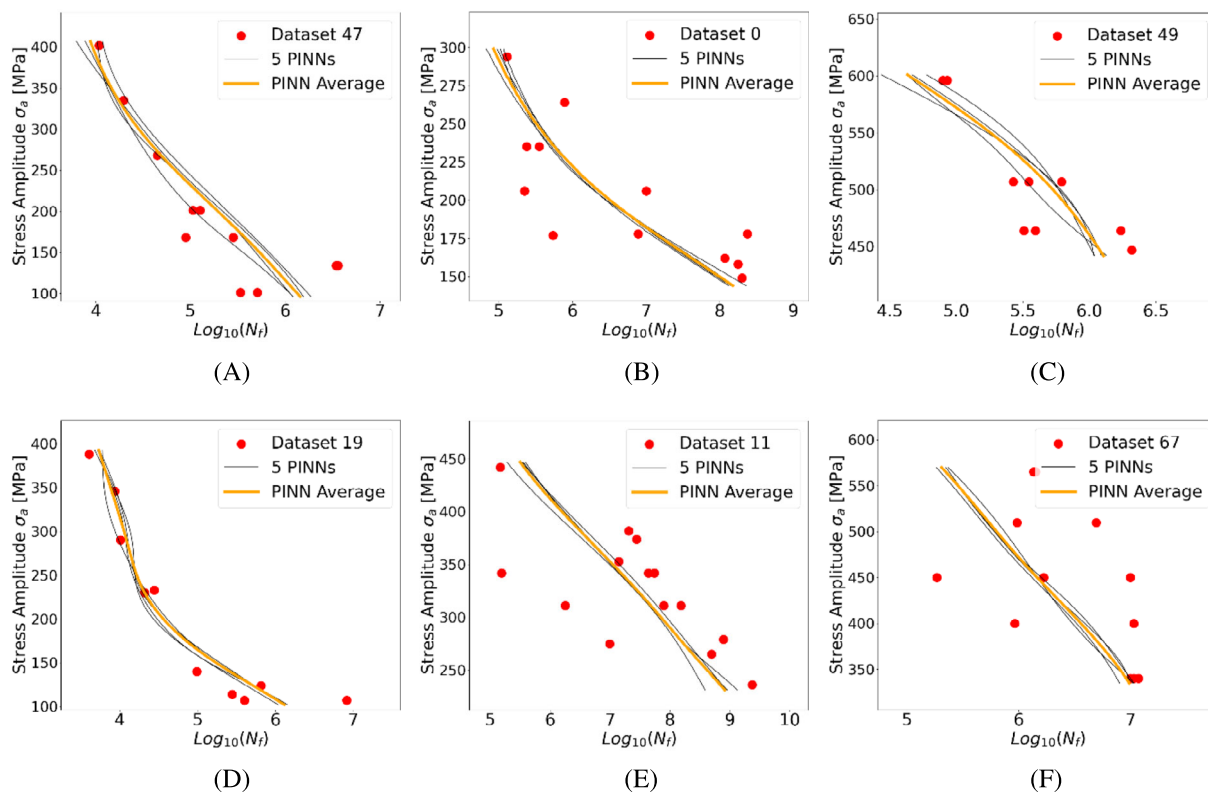


FIGURE 5 Six fatigue curves evaluated with the Physics Informed Neural Network (PINN) algorithm. A mean curve has been generated (orange) from five training sessions (curves in black) for each of the 76 datasets. [Colour figure can be viewed at [wileyonlinelibrary.com](https://onlinelibrary.wiley.com/doi/10.1111/ffem.14254)]

### 3.3 | BLFFNN bilinear predictions

According to Section 2.5, the outputs of the BLFFNN are the four coefficients  $m_1$ ,  $m_2$ ,  $q_1$ , and  $q_2$ , used in the bilinear formulation for the S-N curves modeling  $N_f$  as a function of  $\sigma_a$ . In Figure 6, the black dotted S-N curves have been obtained through by fitting the experimental data, whereas the green curves are estimated with the developed BLFFNN. Figure 6A,B show the datasets “Gong2015 SLM-MP 4”<sup>15</sup> and “DuQian2020, set 1,”<sup>5</sup> respectively. Figure 6C represents the set “Alegre2022 as built”<sup>9</sup> whose concavity is finally facing upward thanks to the bi-linear trend enforcement. In Figure 6D, set “Li2016, Hooerweder et al.”<sup>19</sup> is considered, while Figure 6E,F depict “Yan2019 AF”<sup>14</sup> and “Alegre2022 HIP”<sup>9</sup> sets, correspondingly.

Figure 6 proves the effectiveness of this approach with the P-S-N curves showing a strictly decreasing trend, with concavities facing upwards. Moreover, the estimated S-N curves are in agreement with the experimental data, with the bilinear trend being more appropriate for modeling the stress-life relationship of SLM Ti6Al4V alloy. It is worth noting that the estimated S-N curves can show an asymptotic trend, depending on the considered dataset.

Accordingly, this approach can be reliably employed for datasets with a bilinear trend characterized by two curves showing two different slopes, and for datasets with a first linear trend and a flat trend for the second line, that is, with an asymptotic trend.

### 3.4 | General comparison

In this section, the three approaches are compared to investigate their strength and their weaknesses. Figure 7A represents set “Gong2015 SLM MP-4”<sup>15</sup> validated with the three approaches described in the previous sections. The same analysis has been repeated for sets “DuQian2020 set 1”<sup>5</sup> (Figure 7B), “Alegre2022 as built”<sup>9</sup> (Figure 7C), “Li2016, Hooerweder et al.”<sup>19</sup> (Figure 7D), “Alegre2022 HIP”<sup>9</sup> (Figure 7E), “Li2016, Edwards & Ramulu, Machined & Polished”<sup>19</sup> (Figure 7F), “Sanaei2020, AM250, Annealed and Machined”<sup>8</sup> (Figure 7G), “Yan2019, AF”<sup>14</sup> (Figure 7H), and “DuQian2020, set 2”<sup>5</sup> (Figure 7I), respectively. The three investigated methodologies are plotted in Figure 7: in blue the FFNN (trained with the full TDB), in orange the PINN and in green the BLFFNN of Section 2.5.

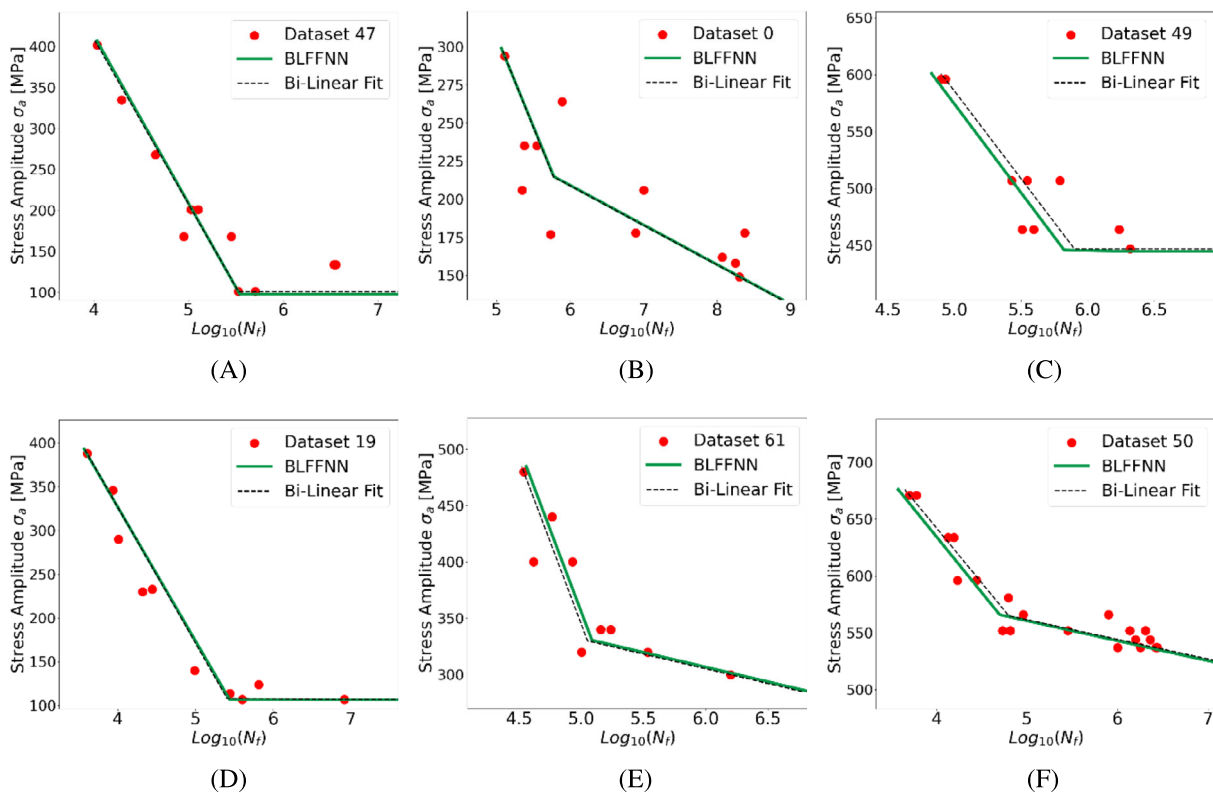
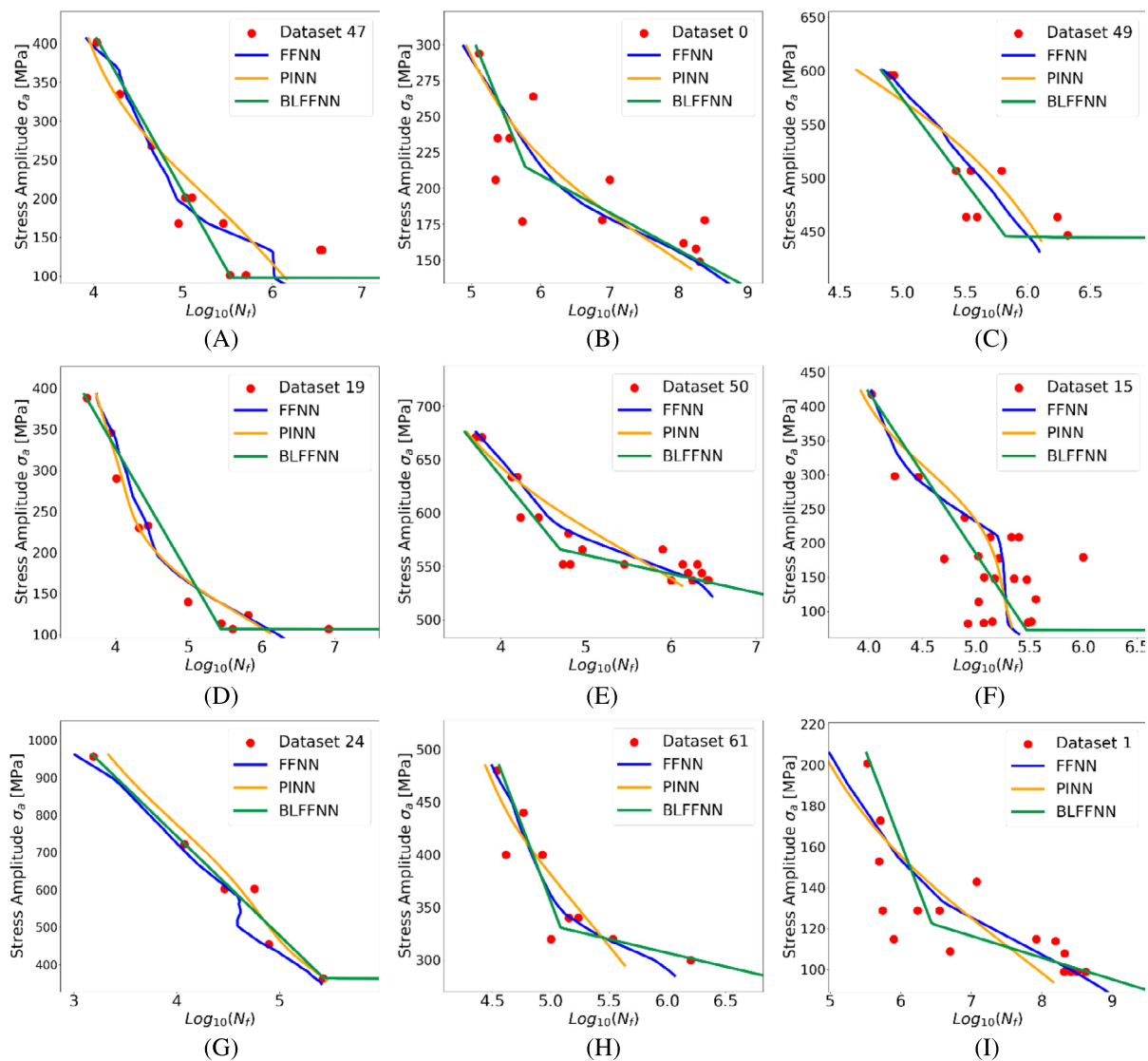


FIGURE 6 Fatigue curves evaluated with the bi-linear feed-forward neural network (BLFFNN). In green the prediction of the BLFFNN, in dotted black the developed bi-linear fit used in the training database. Sets in (A)–(C) are the same shown in Figure 5. [Colour figure can be viewed at [wileyonlinelibrary.com](http://wileyonlinelibrary.com)]



**FIGURE 7** (A–I) Graphical comparison of the techniques seen up to now. It is evident how the BLFFNN delivers better results: in curves (A) and (G) the Feed Forward NN (FFNN) does not have a strictly decreasing behavior, while in c and f the PINN concavity is downward. [Colour figure can be viewed at [wileyonlinelibrary.com](http://wileyonlinelibrary.com)]

According to Figure 7, it can be appreciated how the S-N curves predicted with the BLFFNN provide better estimations, even for datasets for which the other two proposed methods are characterized by bad performance. The S-N curves predicted with the FFNN approach, for example, are in agreement with the experimental data, but tend to overfit, as shown in Figure 7A,B,G. The PINN, moreover, is in agreement with the experimental data, too, but may show a not physical trend, with the concavity facing downward, as shown in Figure 7F,G. On the other hand, the BLFFNN works properly for all datasets, overcoming the criticalities associated with the other two approaches.

### 3.5 | Validation on test datasets

The analyzed methodologies have shown good predicting capabilities for the datasets used for training and their strengths and weaknesses have been highlighted. However, the real fitting capability of these types of algorithms can be reliably tested and validated by considering datasets not used for the training. In Figure 8 the black data points have been considered within the TDB, whereas the colored datasets have been removed from the training datasets and considered as test datasets. These datasets belong to the outer boundary of the whole set of data in the S-N plot, thus allowing for a proper

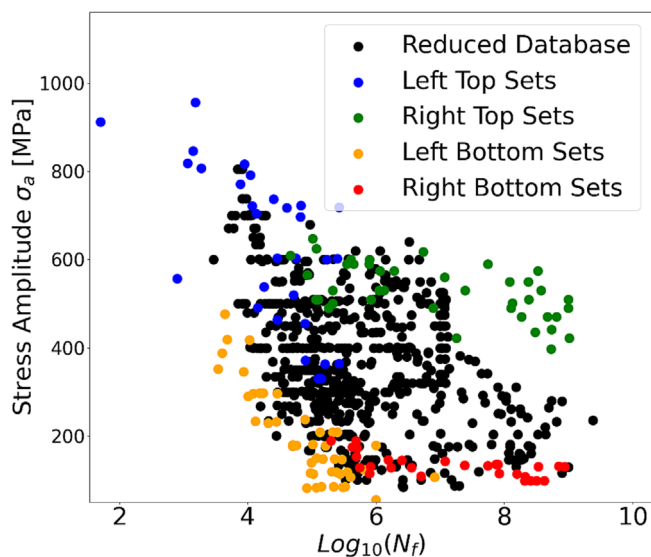


**FIGURE 8** Graphical representation of the Training DataBase (TDB) considered for the validation of the proposed machine learning (ML) algorithms. The points in black are contained inside of it, while the red ones have been removed. Those ones belong to a specific section of the SN diagram highlighted by the respective colored circle, as described in Table 2. [Colour figure can be viewed at [wileyonlinelibrary.com](http://wileyonlinelibrary.com)]

validation. The black points belonging to training datasets are now referred as internal regions of the TDB, whereas the colored datasets are named external regions of the TDB.

Table 3 summarizes the datasets used for this analysis. The number of fatigue points for the training is now reduced from 768 to 620.

Figure 9 plots S-N curves evaluated with test datasets outside of the TDB and curves inside of the TDB in these conditions. Figure 9A reports the external test dataset “DuQian2020, set 7”<sup>5</sup> that belongs to the right-bottom region of the S-N diagram. Figure 9B shows the test set “Sanaei2020, AM250 AB”<sup>8</sup> positioned in the external left-top part of the full S-N diagram. Figure 9C shows the external test set “Li2016, Hooerweder et al.”<sup>19</sup> located in the left-bottom section of the fatigue diagram. The external test dataset “Gunter2017 SLM-2”<sup>6</sup> placed in the right-top part of the S-N diagram, is reported in Figure 9D, whereas in Figure 9E,F the training datasets internal to TDB “Yan2019, AF”<sup>14</sup> and “DuQian2020, set 6,”<sup>5</sup> are shown, respectively.

According to Figure 9, the datasets of the right-bottom and left-top regions have good predicting capabilities. The reason lies behind the fact that they belong to densely populated portions of the SN diagram (Figure 9A,B). The BLFFNN is however having more

difficulties with respect to the other ones as it is more sensitive to the reduction of the number of datasets, since characterized by a smaller number of data available for the training, according to Section 2. For the left-bottom and right-top portions, the performance is moreover scarce (Figure 9C,D). The reason has again to be searched in the physics of fatigue problems: indeed, failures in low life-low stress or high life-high stress regions are unlikely. This leads the TDB to be less crowded in these portions and, consequently, the predictions are poor. This can be expected, since the data for the training in this region is limited; thus, the ML algorithms are forced to make predictions without available data, or with a limited amount of data, for the training. It is worth noting that this validation is very stressful for the developed NN, since, besides considering datasets that rarely occur experimentally, the number of data available for the training has also been reduced. On the other hand, the S-N curves predicted for datasets where a large amount of data for the training is available (Figure 9E,F) are in sound agreement with the experimental data, proving the effectiveness of the methodology and its robustness.

### 3.6 | Blind validation

In this section, the developed ML algorithms have been validated on datasets not considered in the TDB described in Section 2. Accordingly, the number of data available for the training has been kept constant by restoring the TDB to its full capacity, differently from Section 3.5. This validation simulates a real application of the developed ML algorithms, that is, predicting the S-N curves directly from the process parameters and heat and surface treatments without carrying out experimental tests. The three datasets available in Xu et al,<sup>40</sup> have been considered, each one with 20 fatigue points circa, belonging to specimens produced with the same sets of parameters ( $P = 450$  W,  $h = 15$  mm,  $v = 1200$  mm/s,  $t = 50$   $\mu$ m, annealed at  $850^\circ\text{C}$ , machined and polished), but with varying building orientations. Set 1 has  $\vartheta = 90^\circ$ , for set 2,  $\vartheta$  is set to  $45^\circ$ , while for set 3,  $\vartheta = 0^\circ$ . According to Figure 10, the predicted S-N curves are in agreement with the experimental data, proving the robustness and feasibility of the methods.

For set 1 (Figure 10A), the BLFFNN provides the most conservative results, with the S-N curve being below the majority of the experimental failures. On the other hand, for set 2 (Figure 10B) all methods provide good predictions. For set 3 (Figure 10C), the S-N curve predicted with the BLFFNN showed the best performance. Moreover, the data considered for this further validation belongs to poorly populated regions, further confirming



TABLE 3 Validation of the developed NN: testing datasets.

Code	Dataset name	Region	Fatigue properties
1	DuQian2020, set 2 <sup>5</sup>	Right Bottom	High Life
7	DuQian2020, set 8 <sup>5</sup>	(red)	Low Stress
14	Li2016, Edwards & Ramulu As Built <sup>19</sup>	Left Bottom	Low Life
15	Li2016, Edwards & Ramulu Machined and Polished <sup>19</sup>	(yellow)	Low Stress
19	Li2016 Hoerweder et al <sup>19</sup>		
22	Sanaei2020, AM250 Annealed <sup>8</sup>	Left Top	Low Life
23	Sanaei2020, AM250 AB <sup>8</sup>	(blue)	High Stress
24	Sanaei2020, AM250 Annealed and Machined <sup>8</sup>		
25	Sanaei2020, M290 90° Annealed <sup>8</sup>		
26	Sanaei2020, M290 45° Annealed <sup>8</sup>		
27	Sanaei2020, M290 90° AB <sup>8</sup>		
28	Sanaei2020, M290 45° AB <sup>8</sup>		
12	Gunther2017, SLM-26	Right Top	High Life
34	Sun2021, Ultrasonic <sup>22</sup>	(green)	High Stress
35	Sun2021, Rotating Bending <sup>22</sup>		

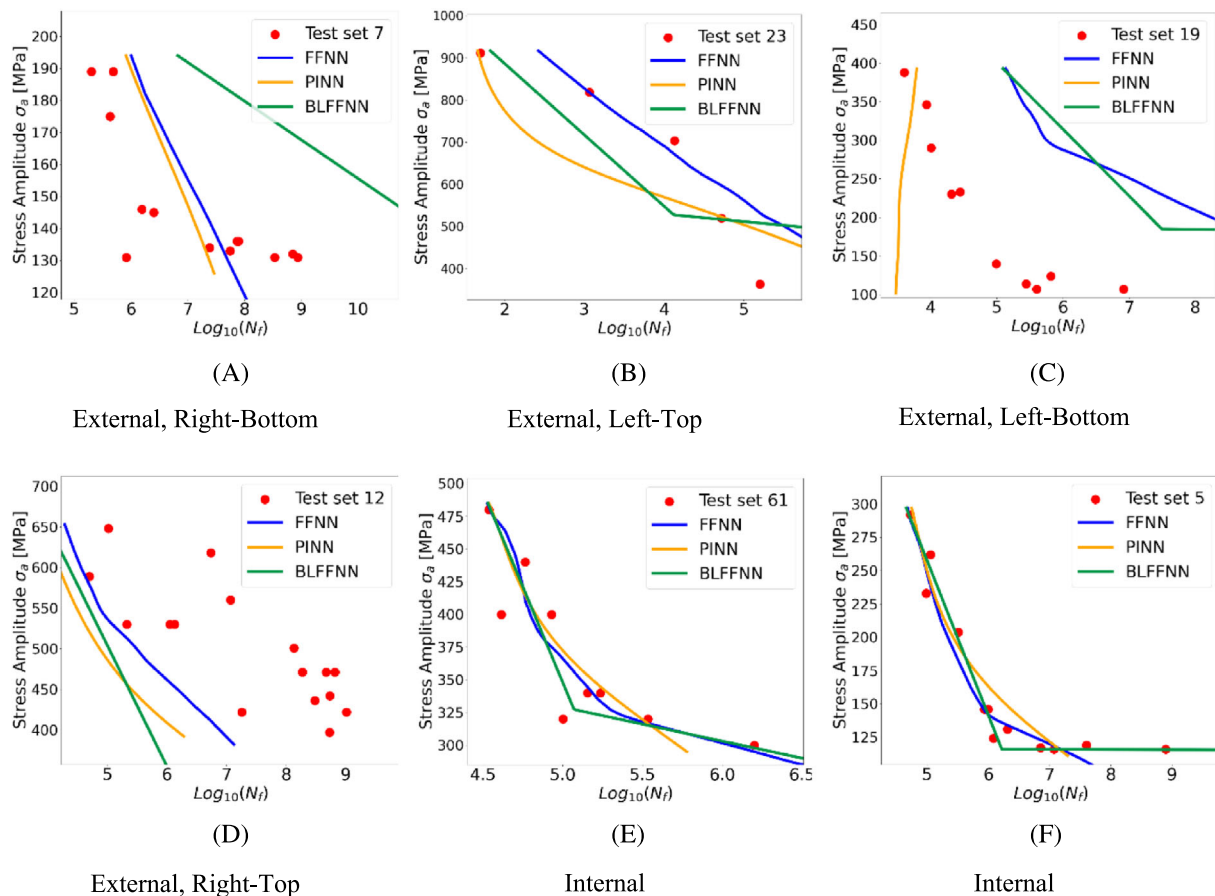
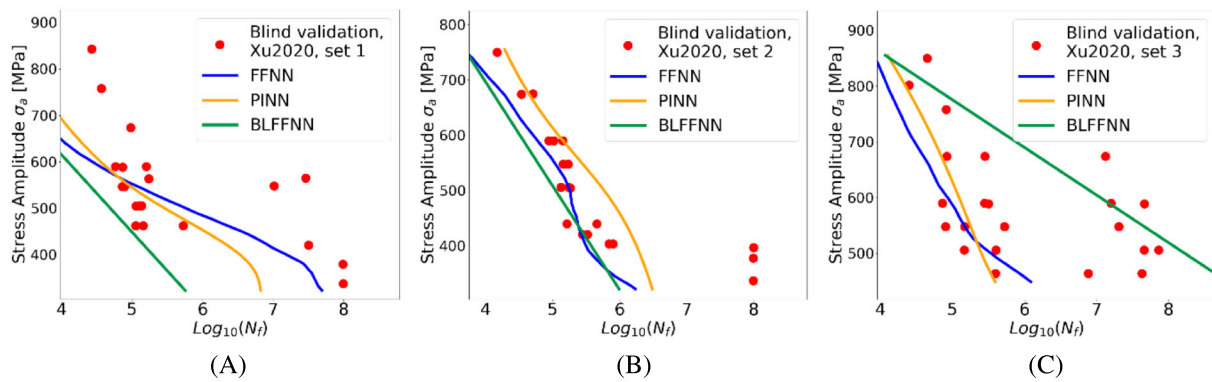


FIGURE 9 Fatigue curves evaluated with the trimmed TDB. (A) The external right-bottom region and (B) the external left-top part; (C) and (D) belong to the left-bottom and right-top portions, and (E) and (F) are in the internal regions. [Colour figure can be viewed at [wileyonlinelibrary.com](https://onlinelibrary.wiley.com/doi/10.1111/ffe.1425)]



**FIGURE 10** Blindly evaluated datasets coming from the article Xu et al.<sup>40</sup> All three sets share the same process parameters except for the building orientation  $\vartheta$ . Set 1 (A) has  $\vartheta = 90^\circ$ , set 2 (B) has  $\vartheta = 45^\circ$ , and for set 3 (C),  $\vartheta = 0^\circ$ . [Colour figure can be viewed at [wileyonlinelibrary.com](http://wileyonlinelibrary.com)]

**TABLE 4** Process parameter variation evaluation database.

	$\vartheta$	$v/P$	$h$	$t$	Ann	T	HIP	Mac	SB	EDM	LSP	SP	SMAT	Pol	$\sigma_a$
1	90	4.8	0.12	40	1	735	0	1	0	0	0	0	0	1	200
2	90	4.8	0.12	40	1	735	0	1	0	0	0	0	0	1	300
3	90	4.8	0.12	40	1	735	0	1	0	0	0	0	0	1	400
4	90	4.8	0.12	40	1	735	0	1	0	0	0	0	0	1	500

the solidity of the networks, since they can perform well enough even in these scarce conditions.

### 3.7 | Process parameters variation validation

Another interesting application of the developed NNs is the analysis of the influence of the process parameters on the fatigue response. In this analysis one process parameter at a time has been varied, while keeping the others constant. Accordingly, it can be verified that the variation of the fatigue response with respect to the investigated process parameter is in agreement with the experimental evidence, even if the interactions between process parameters are not considered. The parameters  $h$ ,  $t$ , and  $v/P$  have been varied. In particular, for each parameter, the constant parameters are equal to the mean for continuous parameters ( $v/P$ ,  $h$  and  $t$ ) or to the most frequent value in case of a discrete parameters (e.g.,  $\vartheta$ , which can only be  $0^\circ$ ,  $45^\circ$ , or  $90^\circ$ ). The same holds for the treatments that, even though they are not varied in this procedure, are set to the most recurrent value (Booleans) or to the average value (e.g., for the heating temperature  $T$ ). Since the NN is outputting  $N_f$ ,  $\sigma_a$  has been set to 200, 300, 400, and 500 MPa respectively, to also highlight

its influence as the studied parameter varies. Table 4 summarizes the database considered for this analysis, with the mean/most frequent parameter kept constant and the varying  $\sigma_a$ . The database is repeated accordingly varying the studied parameter through its range of variation.

Figure 11A shows how the variation of  $h$  affects the life, while for Figure 11B,C the impact of  $t$  and of the cross-parameter  $v/P$  on  $N_f$  is studied.

Feature  $h$  varies from values of 50 to 250  $\mu\text{m}$ . Low values of  $h$  give better fatigue performance as opposed to higher ones (Figure 11A). The reason for this trend can be attributed to the fact that small values of  $h$  allow the laser to better bond the powders, as the part undergo a higher number of passes that create partial remelting on the previous pass, that grant a better connection between the two subsequent passages.<sup>36</sup> The parameter  $t$  ranges from 30 to 60  $\mu\text{m}$ . In this case a significant difference between the three curves cannot be appreciated as the difference in  $N_f$  is small as feature  $t$  changes (Figure 11B). Numerically speaking the reason lies behind the fact that this parameter has not a very high correlation coefficient to the fatigue life  $N_f$  (8%, Table 2). Feature cross combination  $v/P$  ranges from 2.5 to 12.5 mm/W.s. Indeed, if the previously modified parameters are reset to their mean values, a decreasing trend for  $v/P$  can be found in

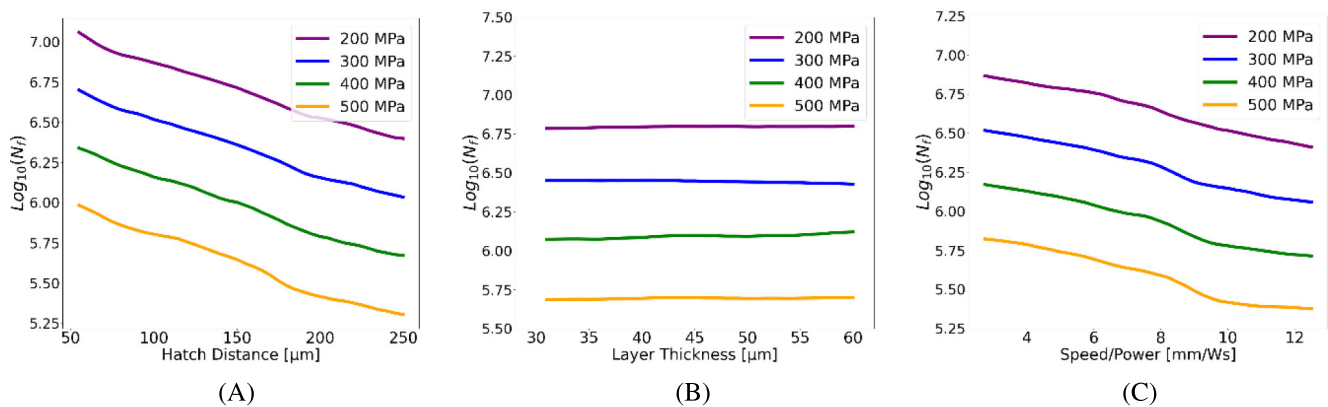


**FIGURE 11** (A–C) Process parameter variation validation. In (A),  $h$  is varied showing a decreasing trend of the life as  $h$  increases. In (B) the small influence of  $t$  on  $N_f$  is reported. In (C) the life decreases as  $v/P$  is increased. [Colour figure can be viewed at [wileyonlinelibrary.com](https://onlinelibrary.wiley.com)]

Figure 11C. The physical reason for this trend is simple. Sufficiently high values of  $P$  allow the powders to melt completely, while low values do not provide enough energy for the bonding. By considering  $v$ , if the laser is traveling too quickly, the material has not sufficient time to create the solidified structure; conversely, if the speed is moderate the powders can have sufficient time to bind with each other.<sup>37</sup> Therefore, it is trivial to understand that if the setup has moderate  $v$  and relatively high  $P$  (low  $v/P$ , e.g., 2.5 mm/W-s) the quality of the finished part could likely be better with respect to parts manufactured with high  $v$  and low  $P$  (high  $v/P$ , e.g., 12.5 mm/W-s). In fact, in Figure 11C, low values of this parameter produce a better fatigue response with respect to high values.

## 4 | CONCLUSIONS

The present study focuses on a design approach against Additive Manufacturing (AM) fatigue failures from the process parameters, set before production, and the post treatment operations, that are affecting the microscopic characteristics, for example, defects, of the Ti6Al4V alloy. The achievement has been accomplished with Machine Learning (ML) algorithms, that are capable of resulting in trustful stress-life curves from the input process parameters (building orientation, laser power, hatch distance, scanning speed and layer thickness), the heat treatments (annealing, annealing temperature and hot isostatic pressing) and the surface treatments (surface polishing, surface machining, shot peening, laser shot peening, sand blasting, surface mechanical attrition and electric discharge machining). Three types of ML neural

networks (NN) have been developed and trained in this research: a feed-forward neural network (FFNN), a physics-informed neural network (PINN), and a bi-linear feed-forward neural network (BLFFNN). The popular FFNN is widely used, especially for preliminary tunings, as it links the input post treatments and process parameters to the stress-life curves with a black-box approach, since the network is not capable of outlining the physical decreasing behavior of fatigue curves. Therefore, the PINN is employed to inform the algorithm of the inverse relation present between the stress amplitude and the fatigue life, by imposing the stress-life derivative to be negative, favoring strictly decreasing behaviors. To ensure the experimental bi-linear evidence of fatigue curves, the BLFFNN has been designed to mitigate untypical tendencies, by forcing a bi-linear fit that results in either two lines with a knee point or a single line with asymptote. The networks have been trained on experimental datasets gathered from literature fatigue tests conducted on selectively laser melted Ti6Al4V specimens. The three methodologies are set side by side to emphasize the superiority of BLFFNN when the fatigue datasets are all evaluated on training sets and to show their limits when the BLFFNN is validated on test sets that have been removed from the training database extrema, showcasing a more robust predictivity of the PINN. To ensure the validity of the techniques, three datasets<sup>40</sup> external to the training database have been blindly evaluated by the networks, to confirm the solidity of the methods, as the predictions fall in the range of the experimental failures. This last study confirms the potential of these ML techniques: the fatigue response can be reliably predicted from the process parameter and the treatments, to reduce the need of further

expensive and time-consuming fatigue testing. In addition, these models can be used to enhance the mechanical component design to obtain the best possible fatigue response.

## NOMENCLATURE

$a$	1st derivative custom loss function weight coefficient
AB	As Built
AM	Additive Manufacturing
Ann	Annealing thermal treatment
$b$	overall precision custom loss function weight coefficient
BLFFNN	Bi-Linear Feed Forward Neural Network
EBM	Electron Beam Melting
EDM	Electric Discharge Machining
$f$	Custom Penalization Function
FFNN	Feed Forward Neural Network
$h$	Hatch Distance [mm]
HCF	High Cycle Fatigue
HIP	Hot Isostatic Pressing thermal treatment
LCF	Low Cycle Fatigue
LSP	Laser Shot Peening surface treatment
Mac	Surface Machining treatment
$m_i$	Linear slope coefficient
ML	Machine Learning
MSE	Mean Square Error
$N$	Number of Cycles to Failure - Fatigue Life [Cycles]
$N_f$	Number of Cycles to Failure - Fatigue Life [Cycles]
NN	Neural Network
NNs	Neural Networks
$P$	Laser Power [W]
PINN	Physics Informed Neural Network
Pol	Surface Polishing treatment
$q_i$	Linear Bias Coefficient
$R$	Stress Ratio
ReLU	Rectified Linear Unit activation function
$RMSE(N_p)$	Root Mean Square Error calculated to the Fatigue Life
$S$	Stress Amplitude [MPa]
SB	Sand Blasting surface treatment
SLM	Selective Laser Melting
SLMed	Selectively Laser Melted
SMAT	Surface Mechanical Attrition surface treatment
SP	Shot Peening surface treatment
$T$	Annealing Temperature [ $^{\circ}$ C]
$t$	Layer Thickness [ $\mu$ m]
$Tanh$	Hyperbolic Tangent activation function
TDB	Training Database
$TDB_{mean}$	Training Database column-wise mean

$TDB_{norm}$	Training Database normalized with the z-score formula
$TDB_{stdev}$	Training Database column-wise standard deviation
$v$	Laser Scan Speed [mm/s]
$v/P$	Speed over Power cross parameter [mm/W-s]
VHCF	Very High Cycle Fatigue
$\vartheta$	Building Orientation [ $^{\circ}$ ]
$\sigma_a$	Stress Amplitude [MPa]
$\sigma_m$	Mean Stress [MPa]
$\sigma_{max}$	Maximum Stress [MPa]
$\sigma_{min}$	Minimum Stress [MPa]




## CONFLICT OF INTEREST STATEMENT

The authors declare that they have no known competing financial interests or personal relationships that could have appeared to influence the work reported in this paper.

## DATA AVAILABILITY STATEMENT

The data that support the findings of this study are available from the corresponding author upon reasonable request.

## ORCID

Alessio Centola  <https://orcid.org/0009-0002-3536-6486>  
 Andrea Tridello  <https://orcid.org/0000-0003-3007-3377>  
 Davide Salvatore Paolino  <https://orcid.org/0000-0002-4231-4580>

## REFERENCES

1. Abdel-Aal HA, Nouari M, El Mansori M. Influence of thermal conductivity on wear when machining titanium alloys. *Tribol Int.* 2009;42(2):359-372.
2. Basalah A, Shanjani Y, Esmaeili S, Toyserkani E. Characterizations of additive manufactured porous titanium implants. *J Biomed Mater Res B Appl Biomater.* 2012;100B(7):1970-1979.
3. Yamashita Y, Murakami T, Mihara R, Okada M, Murakami Y. Defect analysis and fatigue design basis for Ni-based superalloy 718 manufactured by selective laser melting. *Int J Fatigue.* 2018;117:485-495.
4. Murakami Y, Masuo H, Tanaka Y, Nakatani M. Defect analysis for additively manufactured materials in fatigue from the viewpoint of quality control and statistics of extremes. *Procedia Structural Integrity.* 2019;19:113-122.
5. Du L, Qian G, Zheng L, Hong Y. Influence of processing parameters of selective laser melting on high-cycle and very-high-cycle fatigue behaviour of Ti-6Al-4V. *Fatigue Fract Eng Mater Struct.* 2021;44(1):240-256.
6. Günther J, Krewerth D, Lippmann T, et al. Fatigue life of additively manufactured Ti-6Al-4V in the very high cycle fatigue regime. *Int J Fatigue.* 2017;94:236-245.
7. Tridello A, Fiochi J, Biffi CA, et al. Effect of microstructure, residual stresses and building orientation on the fatigue

- response up to 109 cycles of an SLM AlSi10Mg alloy. *Int J Fatigue*. 2020;137:105659.
8. Sanaei N, Fatemi A. Analysis of the effect of internal defects on fatigue performance of additive manufactured metals. *Mater Sci Eng a*. 2020;785:139385.
  9. Alegre JM, Díaz A, García R, Peral LB, Cuesta II. Effect of HIP post-processing at 850 °C/200 MPa in the fatigue behavior of Ti-6Al-4V alloy fabricated by selective laser melting. *Int J Fatigue*. 2022;163:107097.
  10. Mertova K, Dzugan J, Roudnicka M. Fatigue properties of SLM-produced Ti6Al4V with various post-processing processes. In: *IOP conference series: materials science and engineering*. Vol.461; 2018.
  11. Jiang Q, Li S, Zhou C, Zhang B, Zhang Y. Effects of laser shock peening on the ultra-high cycle fatigue performance of additively manufactured Ti6Al4V alloy. *Opt Laser Technol*. 2021; 144:107391.
  12. Eric W, Claus E, Shafaqat S, Frank W. High cycle fatigue (HCF) performance of Ti-6Al-4V alloy processed by selective laser melting. *Adv Mat Res*. 2013;816–817:134-139.
  13. Kumar P, Ramamurty U. High cycle fatigue in selective laser melted Ti-6Al-4V. *Acta Mater*. 2020;194:305-320.
  14. Yan X, Yin S, Chen C, et al. Fatigue strength improvement of selective laser melted ti6al4v using ultrasonic surface mechanical attrition. *Mater Res Lett*. 2019;7(8):7-333.
  15. Gong H, Rafi K, Gu H, Janaki Ram GD, Starr T, Stucker B. Influence of defects on mechanical properties of Ti-6Al-4 V components produced by selective laser melting and electron beam melting. *Mater des*. 2015;86:545-554.
  16. Günther J, Leuders S, Koppa P, et al. On the effect of internal channels and surface roughness on the high-cycle fatigue performance of Ti-6Al-4V processed by SLM. *Mater des*. 2018;143: 1-11.
  17. Macallister N, Becker TH. Fatigue life estimation of additively manufactured Ti-6Al-4V: sensitivity, scatter and defect description in damage-tolerant models. *Acta Mater*. 2022;237: 118189.
  18. Soltani-Tehrani A, Habibnejad-Korayem M, Shao S, Haghshenas M, Shamsaei N. Ti-6Al-4V powder characteristics in laser powder bed fusion: the effect on tensile and fatigue behavior. *Addit Manuf*. 2022;51:102584.
  19. Li P, Warner DH, Fatemi A, Phan N. Critical assessment of the fatigue performance of additively manufactured Ti-6Al-4V and perspective for future research. *Int J Fatigue*. 2016;85: 130-143.
  20. Zhao X, Li S, Zhang M, et al. Comparison of the microstructures and mechanical properties of Ti-6Al-4V fabricated by selective laser melting and electron beam melting. *Mater des*. 2016;95:21-31.
  21. Fousová M, Vojtěch D, Doubrava K, Daniel M, Lin CF. Influence of inherent surface and internal defects on mechanical properties of additively manufactured Ti6Al4V alloy: comparison between selective laser melting and electron beam melting. *Materials*. 2018;11(4):11.
  22. Sun C, Chi W, Wang W, Duan Y. Characteristic and mechanism of crack initiation and early growth of an additively manufactured Ti-6Al-4V in very high cycle fatigue regime. *Int J Mech Sci*. 2021;205:106591.
  23. Karakas Ö. Estimation of fatigue life for aluminium welded joints with the application of artificial neural networks. *Materwiss Werksttech*. 2011;42(10):42-893.
  24. Kalayci CB, Karagöz S, Karakaş Ö. Bee colony intelligence in fatigue life estimation of simulated magnesium alloy welds. *Int J Fatigue*. 2019;127:36-44.
  25. Kalayci CB, Karagoz S, Karakas Ö. Soft computing methods for fatigue life estimation: a review of the current state and future trends. *Fatigue Fract Eng Mater Struct*. 2020;43(12):43-2785.
  26. Soyer MA, Kalayci CB, Karakaş Ö. Low-cycle fatigue parameters and fatigue life estimation of high-strength steels with artificial neural networks. *Fatigue Fract Eng Mater Struct*. 2022; 45(12):3764-3785.
  27. Soyer MA, Tüzün N, Karakaş Ö, Berto F. An investigation of artificial neural network structure and its effects on the estimation of the low-cycle fatigue parameters of various steels. *Fatigue Fract Eng Mater Struct*. 2023;46(8):2929-2948.
  28. Sharma A, Chen J, Diewald E, Imanian A, Beuth J, Liu Y. Data-driven sensitivity analysis for static mechanical properties of additively manufactured Ti-6Al-4V. *ASCE-ASME J Risk Uncertainty Eng Syst, Part B: Mech Eng*. 2022;8(1):011108.
  29. Chen J, Liu Y. Fatigue property prediction of additively manufactured Ti-6Al-4V using probabilistic physics-guided learning. *Addit Manuf*. 2021;39:101876.
  30. Hornías J, Béhal J, Homola P, et al. Modelling fatigue life prediction of additively manufactured Ti-6Al-4V samples using machine learning approach. *Int J Fatigue*. 2023;169:107483.
  31. Ciampaglia A, Tridello A, Paolino DS, Berto F. Data driven method for predicting the effect of process parameters on the fatigue response of additive manufactured AlSi10Mg parts. *Int J Fatigue*. 2023;170:107500.
  32. Salvati E, Tognan A, Laurenti L, Pelegatti M, De Bona F. A defect-based physics-informed machine learning framework for fatigue finite life prediction in additive manufacturing. *Mater des*. 2022;222:111089.
  33. Cutolo A, Lammens N, Vanden Boer K, et al. Fatigue life prediction of a L-PBF component in Ti-6Al-4V using sample data, FE-based simulations and machine learning. *Int J Fatigue*. 2023;167:107276.
  34. Wang H, Li B, Xuan FZ. Fatigue-life prediction of additively manufactured metals by continuous damage mechanics (CDM)-informed machine learning with sensitive features. *Int J Fatigue*. 2022;164:107147.
  35. Maleki E, Bagherifard S, Guagliano M. Correlation of residual stress, hardness and surface roughness with crack initiation and fatigue strength of surface treated additive manufactured AlSi10Mg: experimental and machine learning approaches. *J Mater Res Technol*. 2023;24:3265-3283.
  36. Tang M, Pistorius PC. Fatigue life prediction for AlSi10Mg components produced by selective laser melting. *Int J Fatigue*. 2019;125:479-490.
  37. Mukherjee T, DebRoy T. Mitigation of lack of fusion defects in powder bed fusion additive manufacturing. *J Manuf Process*. 2018;36:442-449.
  38. Hu YN, Wu SC, Withers PJ, et al. The effect of manufacturing defects on the fatigue life of selective laser melted Ti-6Al-4V structures. *Mater des*. 2020;192:108708.

39. Raissi M, Perdikaris P, Karniadakis GE. Physics-informed neural networks: a deep learning framework for solving forward and inverse problems involving nonlinear partial differential equations. *J Comput Phys.* 2019;378:686-707.
40. Xu Z, Liu A, Wang X, Liu B, Guo M. Fatigue limit prediction model and fatigue crack growth mechanism for selective laser melting Ti6Al4V samples with inherent defects. *Int J Fatigue.* 2021;143:106008.

**How to cite this article:** Centola A, Ciampaglia A, Tridello A, Paolino DS. Machine learning methods to predict the fatigue life of selectively laser melted Ti6Al4V components. *Fatigue Fract Eng Mater Struct.* 2023;46(11): 4350-4370. doi:[10.1111/ffe.14125](https://doi.org/10.1111/ffe.14125)